# Absence of diode effect in chiral type-I superconductor NbGe₂

Check for updates

Dong Li [1,2,8] ✉, Zouyouwei Lu [1,3,8], Wenxin Cheng[1,3,8], Xiaofan Shi[1,3,8], Lihong Hu[1,3], Xiaoping Ma[1], Yue Liu [1,3], Yuki M. Itahashi[2], Takashi Shitaokoshi[2], Peiling Li[1], Hua Zhang[1], Ziyi Liu [1], Fanming Qu [1,3,4,5], Jie Shen [1,3,4], Qihong Chen [1,3] ✉, Kui Jin [1,3,4,6], Jinguang Cheng [1,3], Jens Hänisch [7], Huaixin Yang[1,3], Guangtong Liu [1,3,4,5] ✉, Li Lu [1,3,4,5], Xiaoli Dong [1,3,4,6], Yoshihiro Iwasa[2] & Jiangping Hu [1,3]

Symmetry elegantly governs the fundamental properties and derived functionalities of condensed matter. For instance, realizing the superconducting diode effect (SDE) demands breaking space-inversion and time-reversal symmetries simultaneously. Although the SDE is widely observed in various platforms, its underlying mechanism remains debated, particularly regarding the role of vortices. Here, we systematically investigate the nonreciprocal transport in the chiral type-I superconductor NbGe₂. Moreover, we induce type-II superconductivity with elevated superconducting critical temperature on the artificial surface by focused ion beam irradiation, enabling control over vortex dynamics in NbGe₂ devices. Strikingly, we observe negligible diode efficiency ($Q < 2\%$) at low magnetic fields, which rises significantly to $Q \sim 50\%$ at high magnetic fields, coinciding with an abrupt increase in vortex creep rate when the superconductivity of NbGe₂ bulk is suppressed. These results unambiguously highlight the critical role of vortex dynamics in the SDE, in addition to the established symmetry rules.

Stemming from the nonreciprocal phenomena in quantum materials[1–3], novel functionalities such as the superconducting diode effect (SDE) have been achieved in prototype devices through symmetry engineering[4]. Analogous to the semiconductor p-n junctions, superconducting diodes carry dissipationless supercurrent in one direction and show finite resistance in the opposite direction. An asymmetry parameter, called the diode efficiency $Q \equiv \frac{|I_c^+ - I_c^-|}{(I_c^+ + I_c^-)/2}$, was introduced to quantify the difference between the opposite critical currents $I_c^+$ and $I_c^-$ in SDE[5]. The SDE is crucial in realizing energy-efficient and quantum-based superconducting circuits, attracting extensive attention from the superconducting electronics community[6]. However, intense controversy has recently emerged regarding the mechanism of SDE[7]. Specifically, mainstream theories suggest that the SDE arises from the intrinsic inequality of Cooper-depairing currents along opposite directions[8–11]. In contrast, the experimentally measured $I_c$ is considered by other groups to be the vortex-depinning current from a practical viewpoint[12] and the SDE is hence thought to originate from the asymmetric vortex pinning potential[7,13–15].

The central question is how to avoid or even regulate the vortex effect in the study of SDE. Vortices are inevitably generated by the negative interface energy in type-II superconductors but are absent in type-I superconductors with positive interface energy[16]. On the other hand, as one kind of non-reciprocal response, the superconducting diodes require intrinsic space-inversion symmetry breaking. Therefore, investigating SDE in chiral type-I superconductors is an elegant method to circumvent the complicated vortex effect. However, both type-I superconductivity and chiral structures are unusual, rendering the overlap extremely rare. The only identified candidates for chiral type-I superconductors are polycrystalline BeAu (space group $P2_13$)[17] and single crystalline NbGe₂ (space group $P6_222/P6_422$)[18] so far. NbGe₂ belongs to the Kramers-Weyl semimetals[19] with a noticeable antisymmetric spin-orbit coupling (SOC) effect[20]. Meanwhile, the chiral symmetry facilitates the formation of a coupled electron-phonon liquid in NbGe₂ below $T' \sim 50$ K[21]. The electron fluid property leads to an ultralow resistivity in NbGe₂ crystals, posing a large obstacle to comprehensively investigating the subtle nonreciprocal charge transport[22,23].

[1]Beijing National Laboratory for Condensed Matter Physics, Institute of Physics, Chinese Academy of Sciences, Beijing, China. [2]RIKEN Center for Emergent Matter Science (CEMS), Wako, Japan. [3]School of Physical Sciences, University of Chinese Academy of Sciences, Beijing, China. [4]Songshan Lake Materials Laboratory, Dongguan, Guangdong, China. [5]Hefei National Laboratory, Hefei, Anhui, China. [6]Key Laboratory for Vacuum Physics, University of Chinese Academy of Sciences, Beijing, China. [7]Institute for Technical Physics, Karlsruhe Institute of Technology, Eggenstein-Leopoldshafen, Germany. [8]These authors contributed equally: Dong Li, Zouyouwei Lu, Wenxin Cheng, Xiaofan Shi. ✉e-mail: dong.li.hs@riken.jp; qihongchen@iphy.ac.cn; gtliu@iphy.ac.cn

This challenge can be overcome by preparing micro-sized devices using the well-established focused ion beam (FIB) technique[24]. FIB offers an excellent method for investigating quantum materials in the mesoscopic regime, particularly for materials like $NbGe_2$ that are incompatible with mechanical exfoliation. Another advantage of FIB devices is their flexibility in tailoring geometry, enabling diverse experimental configurations for transport measurements. Here, we successfully fabricated the $NbGe_2$ devices using FIB and systematically investigated their nonreciprocal transport. An unexpected outcome of FIB milling is the superconducting amorphous NbGe surface, which coincidentally exhibits type-II superconductivity with a superconducting critical temperature $T_c$ higher than that of $NbGe_2$ bulk. This artificial structure allows for the incorporation of vortex dynamics into $NbGe_2$ devices by suppressing the bulk superconductivity. While most nonreciprocal transport results align well with theoretical predictions, the field dependence of diode efficiency $Q$ is in strong contrast to anticipations. The main message of this paper is that the SDE is negligible ($Q < 2\%$) at low field regimes but emerges ($Q$ exceeding $50\%$) at high field regimes, corresponding to the strongly suppressed or activated vortex dynamics. Our study reveals that, in addition to the well-known symmetry rules, the ubiquitous vortex effect plays a nonnegligible and even critical role in realizing the SDE.

## Results and discussion
### Type-I superconductivity in chiral $NbGe_2$

$NbGe_2$ belongs to the hexagonal C40 structural group, with right- and left-handed helix structures along the $c$-axis corresponding to space groups $P6_222$ (No. 180) and $P6_422$ (No. 181), respectively (Fig. 1a). The left-handedness of these two enantiomers in the studied $NbGe_2$ crystal was confirmed using single-crystal diffraction (Supplementary Table 1). Superconductivity in $NbGe_2$ was first found in 1978[25] and has recently been revisited due to its chiral crystal structure[18,20,21,26,27]. Figure 1b shows the temperature-dependent resistivity of a $NbGe_2$ crystal with a residual resistivity ratio RRR = 96. The $T_c$ is consistent across electrical transport ($T_c = 1.96$ K) and magnetic susceptibility measurements ($T_c = 2.01$ K). It is worth noting that the magnetic susceptibility is identical in both the zero-field-cooled (ZFC) and field-cooled (FC) measurements (Fig. 1c). In type-II superconductors, the diamagnetism measured in the FC mode is smaller than that of the ZFC mode due to the trapped vortices. However, it has been confirmed that the superconductivity in $NbGe_2$ exhibits rare type-I behavior[18,20], which is responsible for the absence of the vortex pinning effect in our FC measurement. As the temperature decreases from 1.8 K to 400 mK (Fig. 1d), we observe a crossover in $NbGe_2$ from type-I super-conductivity at low fields to type-II/1 superconductivity at higher fields[28]. The so-called type-II/1 superconductivity significantly differs from the conventional type-II superconductivity, although magnetic flux will penetrate both superconductors. The interaction between flux quanta is attractive, rather than repulsive, in type-II/1 superconductors[29]. This feature strongly suppresses the vortex dynamics in type-II/1 superconductivity, rendering it more like type-I than the conventional type-II superconductivity.

To enhance the charge transport signals, we fabricated micro-sized $NbGe_2$ devices using FIB ("Methods"). As shown in Fig. 2a, we have deliberately designed the $NbGe_2$ device D3 to simultaneously measure the $c$-axis and $a$-axis transport properties. The $a$-axis resistivity is higher than the $c$-axis resistivity in $NbGe_2$, consistent with previous report[21]. As the temperature-dependent resistivity remains consistent between the $NbGe_2$ bulk and $NbGe_2$ devices in their normal states (Fig. 2b), we believe that the transport properties measured in these devices reliably reflect the bulk characteristics of $NbGe_2$ in the normal state. For instance, one of the chirality-induced anomalies in $NbGe_2$ is the coupled electron-phonon liquid[21], leading to a kink feature in the Kohler scaling[30]. We also measured the magnetoresistance and indeed observed similar results in $NbGe_2$ device D1 (Supplementary Fig. 1), demonstrating the high quality of our $NbGe_2$ devices. According to the crystal symmetry, the chirality-induced non-reciprocal transport response $R = R_0[1 + \gamma(\boldsymbol{B} \cdot \boldsymbol{I})]$ appears when $I$ and $B$ are applied along the helix axis[1,31]. And the nonreciprocal coefficient $\gamma = \frac{2R^{2\omega}}{R^\omega BI}$ is obtained by the associated first-harmonic resistance $R^\omega$ and second-harmonic resistance $R^{2\omega}$ in lock-in measurements[32]. Figures 2c and d show the raw data of field dependent $R^{2\omega}/R^\omega$ measured under red $I//B//c$ and black $I//a \perp B//c$ configurations, respectively. The $R^{2\omega}/R^\omega$ data consists of extrinsic



**Fig. 1 | Type-I superconductor $NbGe_2$. a** The chiral crystal structure of $NbGe_2$. The right-handed and left-handed Ge-Ge bond enantiomers are highlighted by blue and red lines, respectively. **b** The temperature dependent resistivity of a $NbGe_2$ crystal up to 300 K. The residual resistivity ratio RRR = $R_{300 K}/R_{5 K}$ = 96. The inset shows a two-terminal resistance under different magnetic fields, in which the superconducting critical temperature $T_c$ is determined as 1.96 K from the onset of the resistance drop. **c** The temperature dependent dc magnetic susceptibility $\chi$ of $NbGe_2$ crystal under the zero-field-cooled (ZFC) and field-cooled (FC) modes with an applied magnetic field of $\mu_0 H = 0.1$ mT. $T_c$ is determined as 2.01 K from the onset of diamagnetism. The inset shows the expulsion of the magnetic flux from type-I superconductors. **d** The isothermal magnetization of $NbGe_2$ crystal from 1.8 K to 400 mK. The data is corrected by the demagnetization factor. The magnetization is expressed as $\mu_0 M$ to align with the external magnetic field $\mu_0 H$.
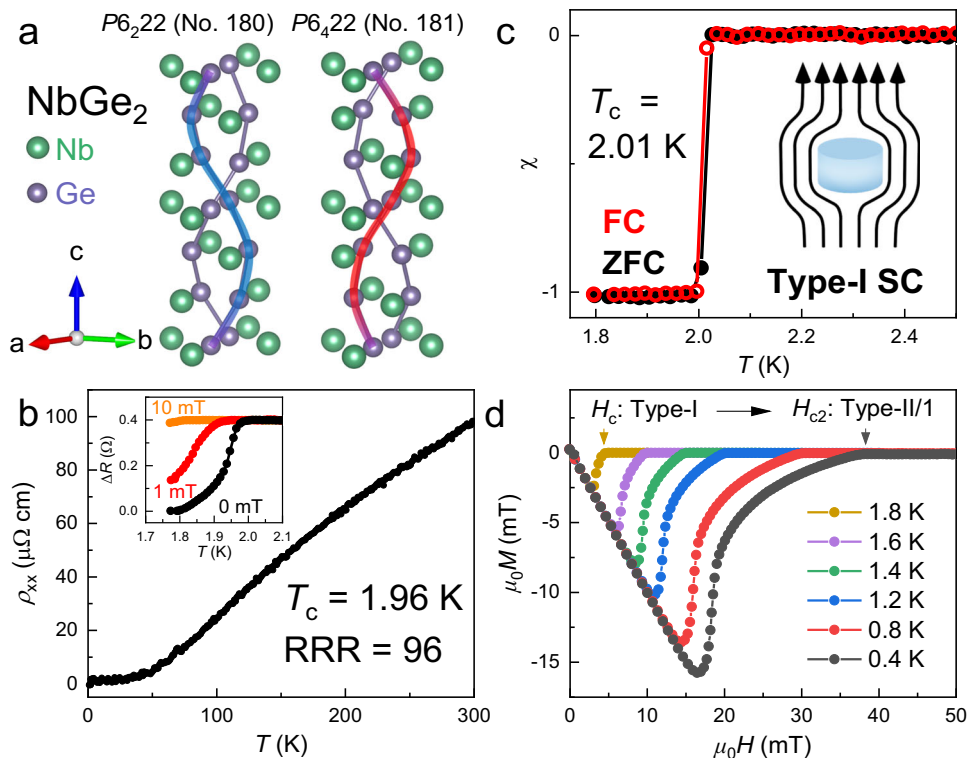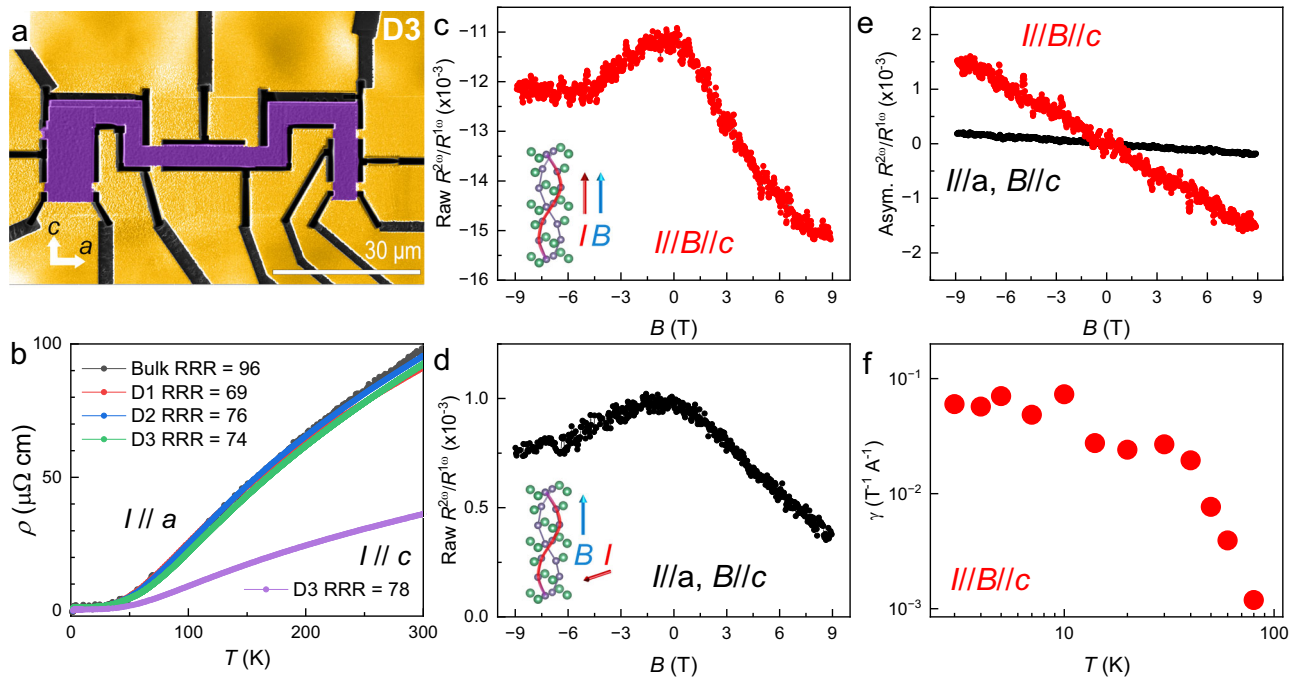
**Fig. 2 | Chirality induced nonreciprocal transport in the normal state of NbGe$_2$.** **a** Scanning electron microscope image of NbGe$_2$ device D3. The NbGe$_2$ microstructures and electrodes are highlighted in purple and yellow colors, respectively. **b** The temperature dependent resistivity of NbGe$_2$ devices D1-D3. The purple $c$-axis transport was obtained from D3. The residual resistivity ratio RRR is calculated from $R_{300\,K}/R_{5\,K}$. **c**, **d** Raw data of field dependence of second-harmonic resistance $R^{2\omega}$/ first-harmonic resistance $R^{1\omega}$ measured under configurations of current $I//$ magnetic field $B//c$-axis and $I \perp B$ at $T = 10$ K, respectively. **e** Asymmetric analysis of the corresponding raw data shown in (**a**, **b**). **f** Temperature dependence of chirality-induced nonreciprocal coefficient $\gamma$ in the normal state. To amplify the subtle $R^{2\omega}$ signal, the applied current was as large as 5 mA. All $R^{2\omega}$ data were obtained on device D3.

symmetric contribution and intrinsic antisymmetric signals. We then extract the intrinsic $R^{2\omega}/R^\omega$ response from the asymmetric part. The $c$-axis nonreciprocal response ($I//B//c$) is significantly stronger than the $a$-axis one ($I//a$, $B//c$) as anticipated (Fig. 2e). With decreasing temperature, the chirality-induced nonreciprocal coefficient $\gamma$ eventually saturates at approximately $7.0 \times 10^{-2}\,T^{-1}\,A^{-1}$ at low temperatures (Fig. 2f), which is of the same order as that observed in the chiral molecular conductor[33]. In principle, the two-fold rotational symmetry ($2_{001}$) prohibits the generation of nonreciprocal response in any direction other than along the $c$-axis. The observation of a tiny $R^{2\omega}$ response along the $a$-axis ($I//a \perp B//c$) suggests the presence of additional symmetry breaking in the NbGe$_2$ device beyond its intrinsic crystal symmetry, potentially arising from the polar symmetry along the $b$-axis of the artificial surface, as discussed below.

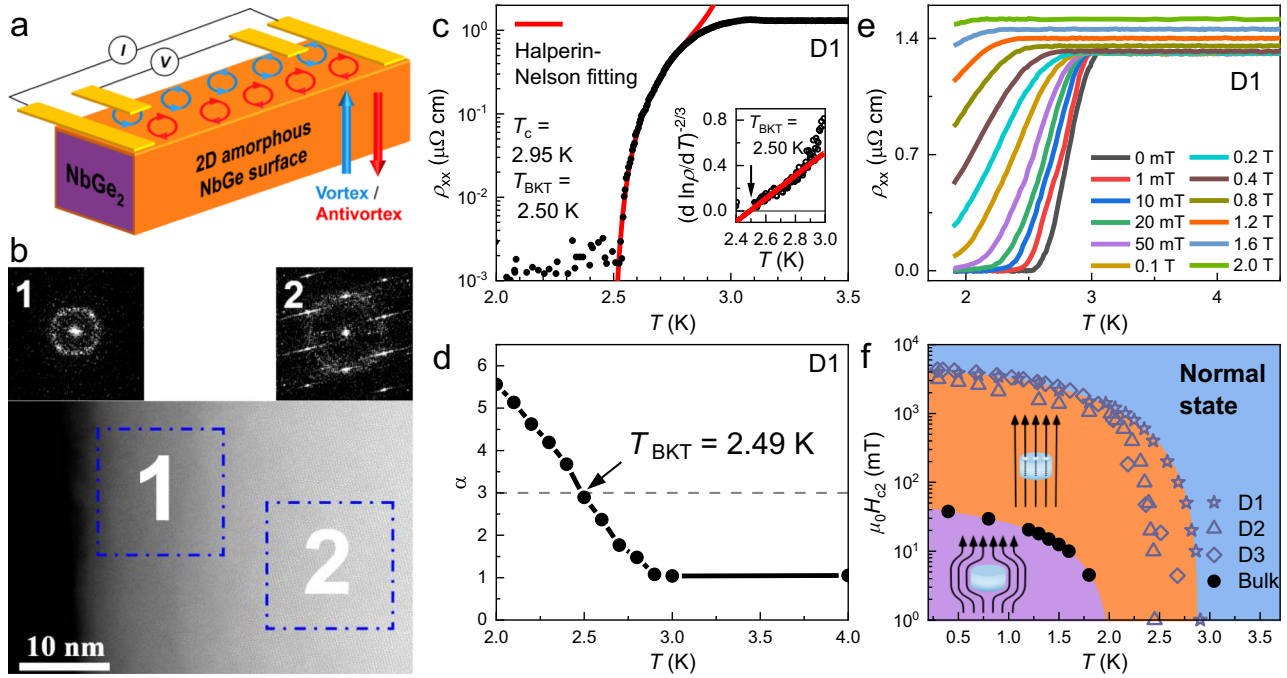**Type-II superconductivity in artificial NbGe surface**

It is well known that the FIB damages the material surface, leaving an artificial amorphous layer due to ion irradiation[24]. The FIB-induced surface damage is gentle and confined to a typical thickness of around 10 nm, ensuring that the transport properties remain unaffected in FIB-fabricated microdevices, as confirmed by our measurement in the normal state (Fig. 2b). However, the situation became complicated when we investigated the superconducting state. As shown in Fig. 3, we found that both $T_c$ and upper critical fields $H_{c2}$ are significantly enhanced from the NbGe$_2$ bulk ($T_c = 2.01$ K, $H_{c2} = 40$ mT) to NbGe$_2$ devices ($T_c = 2.95$ K, $H_{c2} = 4$ T in D1). The enhanced superconductivity originates from the amorphous NbGe surfaces induced by FIB irradiation, as demonstrated by the following observations. Firstly, the scanning transmission electron microscope (STEM) image provides direct evidence of an amorphous surface, with a thickness ranging from 10 to 15 nm (Fig. 3b). The six-fold symmetry is observed in the crystalline region 2 and absent in the amorphous region 1 as expected. The composition of the amorphous surface is identified as NbGe using spatial-resolved electron energy loss spectroscopy (EELS) (Supplementary Fig. 2). Secondly, the broad superconducting resistive transition is

fitted well by the Halperin-Nelson formula[34], showing a Berezinskii-Kosterlitz-Thouless (BKT) transition with a higher $T_c = 2.95$ K in device D1 (Fig. 3c). The fitted BKT transition temperature $T_{BKT}$ in the resistivity is 2.50 K, which is almost identical to $T_{BKT} = 2.49$ K derived from the fitted exponent $V \propto I^\alpha$ at $\alpha\,(T_{BKT}) = 3$ (Fig. 3d). Note that the BKT transitions were reproducibly observed in another NbGe$_2$ device D2 with a different $T_c = 2.50$ K (Supplementary Figs. 3a–d). Lastly, the upper critical fields $H_{c2}$ of NbGe$_2$ device are two orders of magnitude higher than that of NbGe$_2$ bulk (Fig. 3e, f), but are consistent with the $H_{c2}$ of NbGe[35] (Supplementary Note 3). It is anomalous to observe such a considerable enhancement of $H_{c2}$ if the superconductivity comes from NbGe$_2$ bulk.

Based on these results, the amorphous NbGe shell as depicted in Fig. 3a results in enhanced superconducting properties, such as $T_c$ and $H_{c2}$, in transport measurements. Similar amorphous niobium surfaces were created and responsible for the induced superconductivity in non-superconducting NbAs devices via FIB milling[36]. Since twice the superconducting coherence length $2\xi = 32$ nm is larger than the thickness of NbGe surface (see Supplementary Note 4), our results strongly suggest that the NbGe surface hosts 2D superconductivity in NbGe$_2$ devices[37,38]. Additionally, it is worth noting that the vortex dynamics is always absent (strongly suppressed) below the critical field $H_c$ ($H_{c2}$) of NbGe$_2$ due to its type-I (-II/1) superconductivity and its significantly larger cross-section compared to the NbGe surface. However, as confirmed by the observations of BKT transitions, the excitations of vortices/antivortices could penetrate the devices due to the type-II nature of the amorphous NbGe surfaces at higher temperature. This result indicates that we can easily switch between type-I and type-II superconductivity in different regimes, as delineated in the $H$-$T$ phase diagram of Fig. 3f.

**Nonreciprocal transport near $T_c$ in NbGe$_2$ devices**

The amorphous NbGe surface is distinctly separated from the crystalline NbGe$_2$ core, resulting in a well-defined NbGe$_2$/NbGe interface. This sharp boundary is attributed to the self-annealing process occurring at room

**Fig. 3 | Surficial type-II superconductivity in NbGe₂ devices. a** Schematic illustration of NbGe₂ device in the transport measurements. The crystalline NbGe₂ core is covered by a thin amorphous NbGe shield, which induces the excitations of vortex-antivortex pairs. **b** High-angle annular dark field (HAADF) image of focused-ion-beam irradiated NbGe₂. The corresponding fast Fourier transform (FFT) images of the amorphous region 1 and crystalline region 2 are shown in the top panel. **c** Detailed scan of resistivity in device D1 with temperature step of 5 mK. The resistive curve is fitted well by the Berezinskii-Kosterlitz-Thouless (BKT) transition using the Halperin-Nelson formula (red line). The superconducting critical temperature $T_c$ is determined at 90% normal state resistivity $\rho_n$ and the fitted $T_{BKT}$ is 2.50 K. The inset is resistivity replotted on a $[\mathrm{d}(\ln\rho)/\mathrm{d}T]^{-2/3}$ scale. **d** Temperature dependence of the power-law fitted exponent $\alpha$ from zero-field voltage-current ($V$–$I$) curves $V \propto I^\alpha$. The corresponding BKT transition temperature $T_{BKT} \sim 2.49$ K is obtained at $\alpha(T_{BKT}) = 3$. **e** The resistivity of NbGe₂ device D1 as a function of temperature under different magnetic fields. The upper critical field $H_{c2}$ was obtained at 90% $\rho_n$. **f** Superconducting phase diagram of NbGe₂ devices. The solid and open symbols represent the corresponding $H_{c2}$ of NbGe₂ bulk and devices D1–D3, respectively. The regime of type-I (type-II/1) superconductivity of the NbGe₂ core, type-II superconductivity of the NbGe surface, and the normal state are shown in purple, orange, and blue colors, respectively.

temperature[24]. Akin to other artificial interfaces, this interface will induce the Rashba-like SOC, which gives rise to polarization in the perpendicular direction. To investigate this additional space-inversion symmetry breaking, we systematically investigated the nonreciprocal electrical transport in NbGe₂ devices near $T_c$. The polarization-induced second harmonic resistance $R^{2\omega}$ is expressed as $R^{2\omega} \propto (\boldsymbol{P} \times \boldsymbol{B}) \cdot \boldsymbol{I} = -BI\sin\theta$, where $\theta$ represents the angle between the current $I$ and magnetic field $B$ when they are perpendicular to the polarization $P$[22,39]. We indeed observed significant $R^{2\omega}$ responses in NbGe₂ device D2 under the polar configuration of $I \perp B \perp P$ (Fig. 4a) and its typical angular dependence (Fig. 4b). Figure 4c shows the temperature dependence of $\gamma$, which features a peak at $T_{BKT}$ with a value of $3.2 \times 10^5\,\mathrm{T}^{-1}\,\mathrm{A}^{-1}$. Figure 4d illustrates that $R^{2\omega}$ progressively deviates from the anticipated linear behavior in the low-current regime and exhibits a decline in the high-current regime, consistent with previous observations in gated SrTiO₃[40]. Figure 4e, f show the magnetic field dependence of first-harmonic resistance $R^\omega$ and $R^{2\omega}$ at various $T$ down to 0.3 K respectively. It shows that the $R^{2\omega}$ responses are noticeable in the superconducting transition regions but undetectable in the normal state. All the current, temperature, and field dependencies of $R^{2\omega}$ are well reproducible in another NbGe₂ device D1 (Supplementary Fig. 4).

These observations confirm the presence of a polar NbGe₂/NbGe interface, which induces a significant nonreciprocal transport in NbGe₂ devices near $T_c$. There are two major factors that contribute to the substantial increase of $\gamma$ from around $10^{-1}\,\mathrm{T}^{-1}\,\mathrm{A}^{-1}$ in the normal state to approximately $10^5\,\mathrm{T}^{-1}\,\mathrm{A}^{-1}$ in the superconducting state. First, due to the remarkable reduction of the electronic energy scale from Fermi energy to superconducting gap, the $\gamma$ value is gigantically increased when electrons condense into Cooper pairs[41]. The second factor is the BKT transition, which further enhances the $\gamma$ value in the 2D NbGe₂/NbGe interfaces. This

involves a two-step evolution of $\gamma(T)$[41], characterized by $\gamma(T) \sim (T_c - T)$ and $\gamma(T) \sim (T - T_{BKT})^{-3/2}$, as the temperature decreases from $T_c$ to $T_{BKT}$. With a further decreasing $T$, $\gamma$ falls to zero associated with the bound vortex/antivortex pairs in the superconducting ground state. This evolution explains why we observe a peak feature in Fig. 4c. It is worth noting that our observations are highly similar to previous reports in various platforms including gated MoS₂ ($\gamma \sim 8 \times 10^2\,\mathrm{T}^{-1}\,\mathrm{A}^{-1}$)[32], gated SrTiO₃ ($\gamma \sim 3.2 \times 10^6\,\mathrm{T}^{-1}\,\mathrm{A}^{-1}$)[40], Bi₂Te₃/FeTe interfaces (2D $\gamma' \sim 6.5 \times 10^{-3}\,\mathrm{T}^{-1}\,\mathrm{A}^{-1}\,\mathrm{m}$)[42], NbSe₂ antennas ($\gamma \sim 3.4 \times 10^4\,\mathrm{T}^{-1}\,\mathrm{A}^{-1}$)[43], etc. Albeit these materials possess various origins of broken space-inversion symmetry, the theoretical analysis indicated that the nonreciprocal responses are similar in these 2D superconductors due to the BKT transition[41]. Our results show that the motion of unpaired vortices boosts $\gamma$ significantly in NbGe₂ devices, emphasizing the importance of vortex dynamics in nonreciprocal transport[41,44].

## Absence of SDE in type-I NbGe₂ regime

Albeit resistance, whether nonreciprocal or not, vanishes in the superconducting ground state, the supercurrents retain the nonreciprocal characteristics, as manifested itself by the SDE[3]. Owing to a small penetration depth, the theoretical depairing critical current $I_c$ of NbGe₂ is significantly larger than that of the NbGe surface (see Supplementary Note 6). This feature suggests that the superconductivity of NbGe₂ can be detected in terms of $I_c$ (Fig. 5a), in contrast to the $H$-$T$ phase diagram (Fig. 3f), where the superconductivity of NbGe₂ is obscured by the NbGe surface. Hence, the $I$–$V$ characteristics can be divided into two different regimes based on the $H_{c2}$ of NbGe₂: the type-I (or type-II/1) NbGe₂ regime at low magnetic fields and the type-II NbGe regime at high magnetic fields. We characterized the $I$–$V$ curves in both positive and negative directions under different magnetic fields at 0.3 K, and summarized the field dependence of $I_c$ in Fig. 5b. The
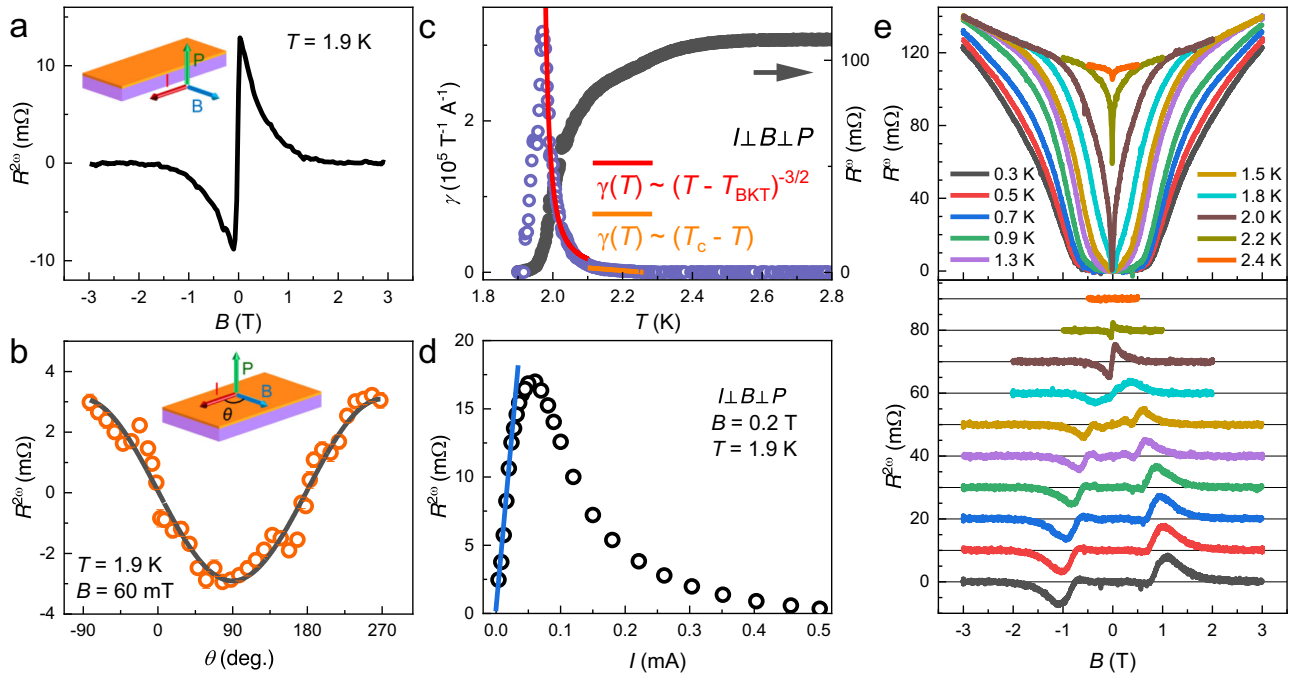
**Fig. 4 | Nonreciprocal transport of a NbGe$_2$ device D2 near the superconducting transition. a** The field dependence of second-harmonic resistance $R^{2\omega}$ at $T = 1.9$ K under polar configuration. Insets show the interfaces between purple NbGe$_2$ bulk and orange NbGe surface. The direction of current $I$ (red arrow), external magnetic field $B$ (blue arrow), and polarization $P$ (green arrow) are perpendicular to each other. **b** Angular dependence of $R^{2\omega}$ measured under 60 mT, 1.9 K. The evolution is fitted well by a gray sine wave. **c** Temperature dependence of the nonreciprocal coefficient $\gamma$ and first-harmonic resistance $R^{\omega}$ near the superconducting transition.

The red and orange fitting line is Berezinskii-Kosterlitz-Thouless (BKT) transition induced nonreciprocal response $\gamma(T) \propto (T - T_{BKT})^{-3/2}$ near BKT transition temperature $T_{BKT}$ and $\gamma(T) \propto (T_c - T)$ near superconducting critical temperature $T_c$. **d** $R^{2\omega}$ as a function of current $I$ at 1.9 K, 0.2 T. The $R^{2\omega}$ is linear with $I$ in the low current region but then gradually deviates the linearity with an increasing $I$. **e** The field dependence of $R^{\omega}$ and $R^{2\omega}$ at various temperatures. The curves of $R^{2\omega}$ are separated vertically by 10 milliohms for clarity.
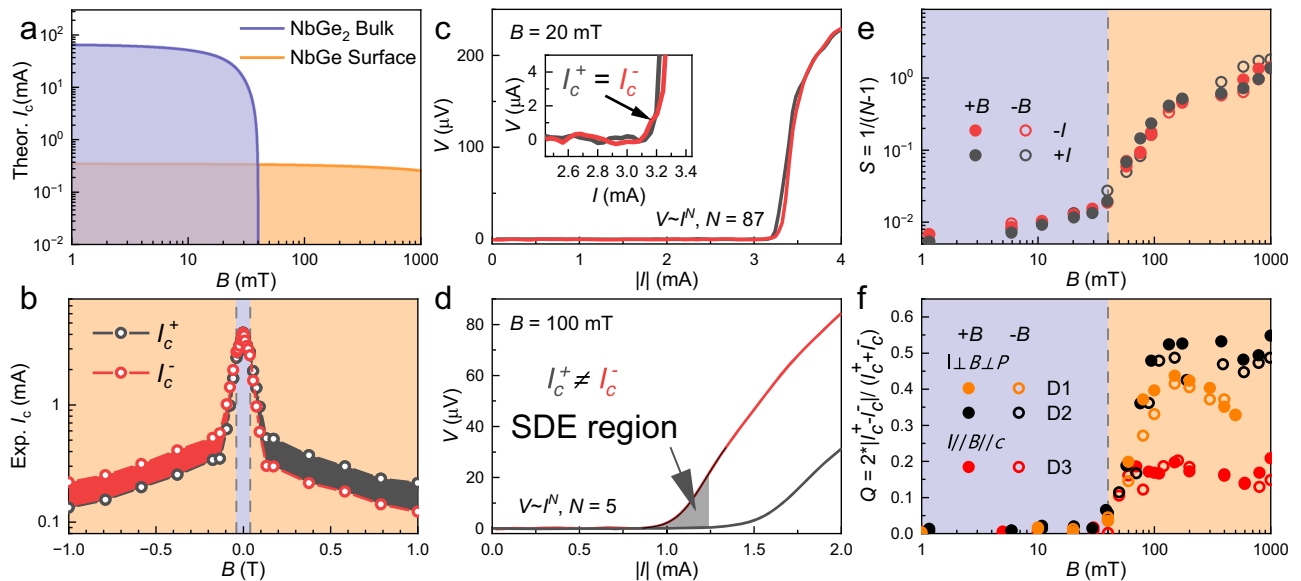


**Fig. 5 | Anomalous field dependence of diode efficiency Q in NbGe$_2$ devices.** **a** Field dependence of theoretical critical current $I_c$ in NbGe$_2$ devices. $I_c$ maximum is calculated from the self-field $I_c$, and the empirical evolution is capped at the measured upper critical field $H_{c2}$. **b** The experimental field dependence of $I_c^+$ (positive direction) and $I_c^-$ (negative direction). The low-field NbGe$_2$ and high-field NbGe regimes are marked by pale purple and orange backgrounds. The opposite polarity of SDE is noted by contrasting red and black colors. **c, d** The typical current-voltage $I$–$V$ curves in low-field NbGe$_2$ and high-field NbGe superconducting regime, respectively. Black and red lines mark the positive and negative current directions. We extract $I_c$ values using the same voltage criterion of 1 μV. The inset of (c) shows an

equal critical current $I_c$ along opposite directions. The SDE was only observed in high-field regime, as marked the gray region in (**d**). **e** The vortex creep rate $S$ as a function of fields. The slope of $S$ changes abruptly as superconductivity transitions from the NbGe$_2$ to NbGe superconducting regime. The solid and open symbols present the data obtained from positive and negative magnetic fields, respectively. **f** The field dependence of $Q$ in NbGe$_2$ devices D1-D3. We measured $I$–$V$ curves under both polar and chiral configurations: current $I \perp$ magnetic field $B \perp$ polarization $P$ (devices D1 and D2) and $I // B // c$-axis (device D3). The $Q$ values are anomalously absent in the NbGe$_2$ superconducting regime.

difference between $I_c^+$ and $I_c^-$ becomes noticeable once $B$ exceeds 40 mT, aligning with the $H_{c2}$ of NbGe$_2$ at 0.3 K. The associated $I$–$V$ curves exhibit clear distinctions between the pale purple NbGe$_2$ regime and the pale orange NbGe regime. In the NbGe$_2$ regime like $B$ = 20 mT, the $I_c$ is equal in opposite directions $I_c^+ = I_c^-$. A tiny nonreciprocity appears in the middle dissipative regime, which is difficult to define as the SDE phenomenon (Fig. 5c). In contrast, when the applied magnetic field increases to 100 mT, $I_c$ becomes distinct along opposite directions, $I_c^+ \neq I_c^-$, showing the emergence of SDE in the NbGe regime (Fig. 5d). One vital functionality of SDE is the perfect rectification effect without dissipation, which is also verified in Supplementary Fig. 5. We notice that its polarity is effectively switched by reversing the magnetic fields, as marked by the contrasting red and gray colors. The switchable polarity of SDE in NbGe$_2$ device is similar to that in polar artificial multilayers[4,45], patterned thin-films[13,15], few-layer NbSe$_2$[46] and others, but in contrast to the strained trigonal superconductor PbTaSe$_2$[47], where the polarity of SDE is fixed and the underlying diode mechanism should be distinct from others.

To characterize the difference in vortex dynamics between NbGe$_2$ and NbGe regimes, we extract the vortex creep rate $S$ using the relation $S \sim 1/(N-1)$, where the flux creep exponent $N$ is derived from $I$–$V$ curves $V(I) \propto I^N$ in the vicinity of $I_c$[48]. Figure 5e displays the corresponding field dependence of $S$, in which the slope of $S$ abruptly increases at the same threshold of 40 mT. This result confirms that the vortex dynamics are strongly suppressed in the NbGe$_2$ regime but effectively activated in the NbGe regime. Additionally, the structural disorder within the amorphous NbGe layer could broaden the $I$–$V$ transition in the type-II regimes (Fig. 5d) compared to the type-I regimes (Fig. 5c). Given that two sources of space-inversion symmetry breaking are observed in NbGe$_2$ devices, we measured $I$–$V$ curves under both configurations: $I \perp B \perp P$ (devices D1 and D2) and $I // B // c$ (device D3). The $I$–$V$ characteristics are highly consistent across different NbGe$_2$ devices, and the field dependence of their diode efficiency $Q$ are shown in Fig. 5f. Distinct from the linear enhancement of $Q$ ($B$) in previous reports of SDE[4,13], the $Q$ value fluctuates within 2% below 40 mT, indicating the absence of SDE even under conditions of simultaneous space-inversion and time-reversal symmetry breaking. The similar evolution of $Q(B)$ and $S(B)$ suggests an underlying relationship between them, highlighting the significance of vortex dynamics in triggering SDE. We also observed small $Q$ values ~ 0.2 when the external magnetic fields were parallel to the currents in device D3, a configuration in which the unidirectional Lorentz force should be absent, and thus the SDE is expected to be negligible. However, the applied currents inevitably generate vortex and antivortex pairs, known as the self-field effect[12]. The excitation of vortex/antivortex pairs could induce giant nonreciprocity even when $B$ = 0[44], providing a possible explanation for our observations in the $B // I$ configuration.

## Conclusions

In summary, we systematically performed nonreciprocal transport measurements on FIB fabricated NbGe$_2$ devices and confirmed the critical role of vortex dynamics in realizing a significant SDE. By inducing artificial NbGe surfaces through FIB irradiation, we observed enhanced superconductivity in these devices. Both types of space-inversion symmetry breaking, chirality in the NbGe$_2$ bulk and polarization at the NbGe$_2$/NbGe interface, were detected in the nonreciprocal transport measurements. Additionally, two-dimensional vortex excitations emerged on the NbGe surfaces as the type-I superconductivity of NbGe$_2$ bulk was suppressed, leading to the BKT transition and a dramatic increase in the nonreciprocal coefficient. The SDE was negligible in the NbGe$_2$ bulk at low magnetic fields but became pronounced in the NbGe surface under high magnetic fields, aligning with the abrupt increase in vortex creep rates.

Although we did not observe the SDE in chiral NbGe$_2$, likely due to the weak antisymmetric SOC, we cannot dismiss the possibility of exotic superconductivity induced SDE, such as the finite momentum Cooper pairing[49]. Due to the inevitable excitation of vortices in type-II superconductors, it is challenging to distinguish between contributions to SDE from intrinsic crystal symmetry and those from extrinsic vortex effects. Therefore, it is crucial to exercise caution when attributing the widely

observed SDE to the inherent symmetry breaking in superconductivity, rather than to the artificial asymmetry. Additional phase-sensitive experiments, such as those measuring the interference patterns[50] or Little–Parks oscillations[51], are necessary and promising to support the existence of exotic superconductivity in these platforms.

From the perspective of electronic applications, we have confirmed that artificial superconducting surfaces can host the SDE. This functionality can be readily replicated in various quantum materials containing superconducting elements, such as niobium, using FIB technology. Consequently, we envision a significant expansion of the SDE application into a broader range of electronic devices, including potential integration with non-superconducting quantum materials, such as the Weyl semimetal NbAs. Our findings suggest that the unique properties of these materials could be harnessed in conjunction with SDE to develop advanced electronic components with enhanced performance and functionality.

## Methods

### Crystal synthesis and characterizations

NbGe$_2$ single crystals were synthesized by vapor transport using iodine as the transport agent. At first, the polycrystalline NbGe$_2$ samples, prepared via solid-state reaction at a heating temperature of 850 °C, were ground into a powder and mixed with iodine in a glove box. The reactants were then sealed under vacuum in a quartz tube and placed in a two-zone furnace, with the hot end maintained at 850 °C and the cold end at 800 °C. After two weeks, hexagonal crystals with typical sizes of 0.5 mm × 0.5 mm × 0.3 mm were obtained after ultrasonic cleaning in ethanol. Magnetization measurements were performed in a Quantum Design MPMS-XL system. The isothermal magnetization down to 400 mK was collected in an MPMS-3 system equipped with the He3 option. The NbGe$_2$ crystal structures are drawn by VESTA[52].

### Devices fabrication

All NbGe$_2$ devices were fabricated by a FEI Helios-600i FIB under an acceleration voltage of up to 30 kV with Ga ion sources. Similar to the methods developed by Moll et al.[24], the whole procedure of FIB device preparation can be summarized as four steps.

**First step: preparing the lamella from bulk samples**. The crystallographic orientation of the NbGe$_2$ bulk was checked by the Laue diffraction and mounted in the SEM sample holder. We then cut the lamella with a typical size of 150 × 40 × 2 μm$^3$ from bulk like the routine sample preparation for the transmission electron microscope. A high 65 nA was used to dig the grooves, and a smaller current of 2.5 nA was then used to polish the sidewalls into a flat shape under grazing incidence.

**Second step: transferring the lamella to substrate**. Firstly, we place a hundred-micrometer-sized droplet of Araldite epoxy glue on the sapphire substrate with lithographically prepatterned gold contact pads. We vertically picked up the lamellas from crystals and then horizontally, flat sides down, put them onto the droplet using an ex-situ micromanipulator. The continuous and smooth contacting profile between lamella and droplet was built by the capillary forces of epoxy liquid.

**Third step: evaporating gold electrical contacts**. The droplet was first heated at 150 °C for one hour to release the bubble from the epoxy droplet. A brief argon etching was used to clean the surface of the lamellas before the following gold evaporation. By using a homemade shadow mask, typical Ti/Au (5/300 nm) layers were deposited on the region covering lamellas and contact pads. The deposited gold layers serve as the electrical contacts with a typical contact resistance of a few Ohms.

**Final step: shaping the measured region**. We put the substrate with covered lamellas back into the FIB chamber and proceeded with the final cutting. The covered gold layers were carefully removed by FIB milling at 1.6 nA, 5 kV. Then, the overall shape of the measured region and the

position of the corresponding contact was cut by FIB at 0.79 nA, 30 kV. Finally, the outer gold layer is selectively cut through to ensure the applied current flows only as designed for transport measurements.

### STEM on amorphous surfaces

To characterize the FIB induced amorphous damage, STEM specimens were prepared using the same FIB machine with the same milling parameters as those used for $NbGe_2$ devices. Atomically resolved high-angle annular dark-field scanning transmission electron microscopy (HAADF-STEM) and electron energy loss spectroscopy (EELS) were conducted on a JEOL ARM200F transmission electron microscopy (TEM) equipped with a probe-forming spherical-aberration corrector.

### Electrical transport measurements

The temperature-dependent resistance and magnetoresistance were conducted in a Quantum Design PPMS-9 system. The dc $I–V$ measurements were collected by two Keithley meters 6221 and 2182. The ac $R^{\omega}$ and $R^{2\omega}$ were obtained by the Stanford SR830 lock-in amplifiers with a frequency of 137.77 Hz, and a phase offset as $-90°$ was set to collect $R^{2\omega}$ in the non-reciprocal transport measurements. To obtain a higher cooling power during the current-voltage measurements at 300 mK, similar transport measurements were performed in a top-loading He-3 refrigerator with a 15 T superconducting magnet.

Note added: We noticed a similar study on FIB fabricated $NbGe_2$ device during the peer review process[53].

## Data availability

The data that support the plots within this paper and other finding of this study are available from the corresponding author upon reasonable request.

## References

1. Tokura, Y. & Nagaosa, N. Nonreciprocal responses from non-centrosymmetric quantum materials. *Nat. Commun.* **9**, 3740 (2018).
2. Ideue, T. & Iwasa, Y. Symmetry breaking and nonlinear electric transport in van der Waals nanostructures. *Annu. Rev. Condens. Matter Phys.* **12**, 201 (2021).
3. Nagaosa, N. & Yanase, Y. Nonreciprocal transport and optical phenomena in quantum materials. *Annu. Rev. Condens. Matter Phys.* **15**, 63 (2024).
4. Ando, F. et al. Observation of superconducting diode effect. *Nature* **584**, 373 (2020).
5. He, J. J., Tanaka, Y. & Nagaosa, N. J. N. Jo. P. A phenomenological theory of superconductor diodes. *N. J. Phys.* **24**, 053014 (2022).
6. Nadeem, M., Fuhrer, M. S. & Wang, X. The superconducting diode effect. *Nat. Rev. Phys.* **5**, 558 (2023).
7. Moll, P. J. W. & Geshkenbein, V. B. Evolution of superconducting diodes. *Nat. Phys.* **19**, 1379 (2023).
8. Daido, A., Ikeda, Y. & Yanase, Y. Intrinsic superconducting diode effect. *Phys. Rev. Lett.* **128**, 037001 (2022).
9. Yuan, N. F. Q. & Fu, L. Supercurrent diode effect and finite-momentum superconductors. *Proc. Natl Acad. Sci. USA* **119**, e2119548119 (2022).
10. Jiang, K. & Hu, J. Superconducting diode effects. *Nat. Phys.* **18**, 1145 (2022).
11. Ilic, S. & Bergeret, F. S. Theory of the supercurrent diode effect in Rashba superconductors with arbitrary disorder. *Phys. Rev. Lett.* **128**, 177001 (2022).
12. Kwok, W. K. et al. Vortices in high-performance high-temperature superconductors. *Rep. Prog. Phys.* **79**, 116501 (2016).
13. Hou, Y. et al. Ubiquitous superconducting diode effect in superconductor thin films. *Phys. Rev. Lett.* **131**, 027001 (2023).
14. Gutfreund, A. et al. Direct observation of a superconducting vortex diode. *Nat. Commun.* **14**, 1630 (2023).
15. Lyu, Y. Y. et al. Superconducting diode effect via conformal-mapped nanoholes. *Nat. Commun.* **12**, 2703 (2021).
16. Tinkham, M. *Introduction to superconductivity* (Courier Corporation, 2004), Vol. 1.
17. Amon, A. et al. Noncentrosymmetric superconductor BeAu. *Phys. Rev. B* **97**, 014501 (2018).
18. Lv, B. et al. Type-I superconductivity in noncentrosymmetric NbGe2. *Phys. Rev. B* **102**, 064507 (2020).
19. Chang, G. et al. Topological quantum properties of chiral crystals. *Nat. Mater.* **17**, 978 (2018).
20. Emmanouilidou, E. et al. Fermiology and type-I superconductivity in the chiral superconductor NbGe2 with Kramers-Weyl fermions. *Phys. Rev. B* **102**, 235144 (2020).
21. Yang, H. Y. et al. Evidence of a coupled electron-phonon liquid in NbGe2. *Nat. Commun.* **12**, 5292 (2021).
22. Ideue, T. et al. Bulk rectification effect in a polar semiconductor. *Nat. Phys.* **13**, 578 (2017).
23. Wang, Y. et al. Gigantic magnetochiral anisotropy in the topological semimetal ZrTe5. *Phys. Rev. Lett.* **128**, 176602 (2022).
24. Moll, P. J. W. Focused ion beam microstructuring of quantum matter. *Annu. Rev. Condens. Matter Phys.* **9**, 147 (2018).
25. Remeika, J., Cooper, A., Fisk, Z. & Johnston, D. Superconductivity of single-crystal NbGe2. *J. Less-Common Met.* **62**, 211 (1978).
26. Sato, Y. J. et al. Fermi surface topology and electronic transport properties of chiral crystal NbGe2 with strong electron-phonon interaction. *Phys. Rev. B* **108**, 235115 (2023).
27. Yao, M. et al. Observation of chiral surface state in superconducting NbGe2. *arXiv: 2403.03324* (2024).
28. Zhang, D. et al. Full superconducting gap and type-I to type-II superconductivity transition in single crystalline NbGe2. *Phys. Rev. B* **103**, 214508 (2021).
29. Kimura, N. et al. Type II/1 superconductivity with extremely high Hc3 in noncentrosymmetric LaRhSi3. *J. Phys. Soc. Jpn.* **85**, 024715 (2016).
30. Xu, J. et al. Extended Kohler's rule of magnetoresistance. *Phys. Rev. X* **11**, 041029 (2021).
31. Rikken, G. L., Folling, J. & Wyder, P. Electrical magnetochiral anisotropy. *Phys. Rev. Lett.* **87**, 236602 (2001).
32. Wakatsuki, R. et al. Nonreciprocal charge transport in noncentrosymmetric superconductors. *Sci. Adv.* **3**, e1602390 (2017).
33. Pop, F., Auban-Senzier, P., Canadell, E., Rikken, G. L. & Avarvari, N. Electrical magnetochiral anisotropy in a bulk chiral molecular conductor. *Nat. Commun.* **5**, 3757 (2014).
34. Halperin, B. I. & Nelson, D. R. Resistive transition in superconducting films. *J. Low. Temp. Phys.* **36**, 599 (1979).
35. Berghuis, P. & Kes, P. H. Two-dimensional collective pinning and vortex-lattice melting in a-Nb1−xGex films. *Phys. Rev. B* **47**, 262 (1993).
36. Bachmann, M. D. et al. Inducing superconductivity in Weyl semimetal microstructures by selective ion sputtering. *Sci. Adv.* **3**, e1602983 (2017).
37. Li, D. et al. Quasi-two-dimensional nature of high-Tc superconductivity in iron-based (Li,Fe)OHFeSe. *Chin. Phys. Lett.* **39**, 127402 (2022).
38. Saito, Y., Nojima, T. & Iwasa, Y. Highly crystalline 2D superconductors. *Nat. Rev. Mater.* **2**, 16094 (2016).
39. Rikken, G. L. & Wyder, P. Magnetoelectric anisotropy in diffusive transport. *Phys. Rev. Lett.* **94**, 016601 (2005).
40. Itahashi, Y. M. et al. Nonreciprocal transport in gate-induced polar superconductor SrTiO3. *Sci. Adv.* **6**, eaay9120 (2020).
41. Hoshino, S., Wakatsuki, R., Hamamoto, K. & Nagaosa, N. Nonreciprocal charge transport in two-dimensional noncentrosymmetric superconductors. *Phys. Rev. B* **98**, 054510 (2018).
42. Yasuda, K. et al. Nonreciprocal charge transport at topological insulator/superconductor interface. *Nat. Commun.* **10**, 2734 (2019).
43. Zhang, E. et al. Nonreciprocal superconducting NbSe2 antenna. *Nat. Commun.* **11**, 5634 (2020).

44. Itahashi, Y. M. et al. Giant second harmonic transport under time-reversal symmetry in a trigonal superconductor. *Nat. Commun.* **13**, 1659 (2022).
45. Narita, H. et al. Field-free superconducting diode effect in noncentrosymmetric superconductor/ferromagnet multilayers. *Nat. Nanotechnol.* **17**, 823 (2022).
46. Bauriedl, L. et al. Supercurrent diode effect and magnetochiral anisotropy in few-layer NbSe(2). *Nat. Commun.* **13**, 4266 (2022).
47. Liu, F. et al. Superconducting diode effect under time-reversal symmetry. *Sci. Adv.* **10**, eado1502 (2024).
48. Hänisch, J. et al. Anisotropy of flux pinning properties in superconducting (Li,Fe)OHFeSe thin films. *Supercond. Sci. Technol.* **33**, 114009 (2020).
49. Pal, B. et al. Josephson diode effect from Cooper pair momentum in a topological semimetal. *Nat. Phys.* **18**, 1228 (2022).
50. Le, T. et al. Superconducting diode effect and interference patterns in kagome CsV(3)Sb(5). *Nature* **630**, 64 (2024).
51. Wan, Z. et al. Unconventional superconductivity in chiral molecule-TaS(2) hybrid superlattices. *Nature* **632**, 69 (2024).
52. Momma, K. & Izumi, F. VESTA 3 for three-dimensional visualization of crystal, volumetric and morphology data. *J. Appl. Crystallogr.* **44**, 1272 (2011).
53. Bai, Z. et al. Negative magnetoresistance component and supercurrent diode effect in microstructured NbGe2 chiral crystals. *Phys. Rev. B* **110**, 214507 (2024).

## Acknowledgements

## Author contributions

D. Li conceived this project. Crystals were synthesized and characterized by Z.-Y.W.L., D.L., Y.L., T.S., X.-L.D., and J.-G.C. The FIB devices were prepared by D.L., W.-X.C., X.-F.S., and J.S. The electrical transport measurements were conducted by D.L., L.-H.H., W.-X.C., T.S., P.-L.L., H.Z., Z.-Y.L., Q.-H.C., K.J., F.-M.Q., and G.-T.L. TEM experiments were performed and analyzed by X.-P.M. and H.-X.Y. The experimental results were analyzed by D.L., Y.M.I., J.H., and Y.I. D.L., Q.-H.C., and G.-T.L. wrote the manuscript with input from all authors. X.-L.D., K.J., J.-G.C., H.-X.Y, Li Lu, J.-P. Hu, and Y.I. coordinated this research project.

## Competing interests

The authors declare no competing interests.

## Additional information